A finite strain viscoelastic model with damage and tension-compression asymmetry considerations for solid propellants

F. Gouhier[a], J. Diani[a], A. Vandenbroucke[b]

[a]*Laboratoire de Mécanique des Solides,UMR 7649, École Polytechnique, 91128 Palaiseau, France*
[b]*ArianeGroup SAS, Centre de Recherche du Bouchet, 9 rue Lavoisier, 91710 Vert-le-Petit, France*

Abstract

A short survey on the experimental testing of solid propellants has highlighted finite strain responses that are temperature-dependent, viscoelastic with damage, and exhibit tension/compression asymmetry. Consequently, a finite strain viscoelastic model that satisfies the principles of thermodynamics has been developed. This model is based on the common multiplicative decomposition of the deformation gradient into elastic and viscous components, with considerations for damage and asymmetry. The model has been tested against three sets of data from the literature, carefully selected to represent the various characteristics of solid propellants. The model accurately reproduces uniaxial tension responses at different strain rates and temperatures, with the capability to account for superimposed hydrostatic pressure. Notably, these satisfactory representations require only five fitting parameters, in addition to the typical identification of polymer linear viscoelasticity and time-temperature superposition. Finally, an attempt to reproduce both tension and compression tests conducted independently on the same material underscores the need to account for tension-compression asymmetry, as defined in the proposed constitutive equations. This finding advocates for new tests, such as compression following tension and vice versa.

Keywords: Constitutive model, Finite strain, Viscoelasticity, Damage, Tension-compression asymmetry, Propellant

Email addresses: florian.gouhier@polytechnique.edu (F. Gouhier), julie.diani@polytechnique.edu (J. Diani), aude.vandenbroucke@ariane.group (A. Vandenbroucke)

1. Introduction

Solid propellants are made of amorphous rubbery binders heavily filled with energetic particles that vary in size from a few to several hundred microns. Their applications cover solid rockets, explosives, automobile airbags... (Davenas, 2003). The amorphous polymer network may undergo large strains, but damage at the binder/filler interface (Tao et al., 2013; de Francqueville et al., 2021) develops early during stretching, leading to significant material softening (Swanson and Christensen, 1983).

Early viscoelastic models for propellants were developed using either infinitesimal strain (Park and Schapery, 1997; Ha and Schapery, 1998; Duncan and Margetson, 1998) or finite strain (Özüpek and Becker, 1992, 1997) based on the constitutive equations of Simo (1987). The constitutive equations proposed by Özüpek and Becker (1997) are the most commonly used and extended (Jung and Youn, 1999; Jung et al., 2000; Canga et al., 2001; Yıldırım and Özüpek, 2011; Yun et al., 2016; Tunç and Özüpek, 2016; Kumar et al., 2019; Kantor et al., 2021; Wubuliaisan et al., 2023b), despite concerns about their thermodynamic consistency (Govindjee et al., 2014). Finite strain viscoelastic constitutive equations based on the multiplicative decomposition of the deformation gradient (Sidoroff, 1974), originally developed for rubbers (Le Tallec et al., 1993; Lion, 1997; Reese and Govindjee, 1998), have rarely been proposed for propellants. One notable recent contribution is by Kumar et al. (2018), based on the rubber model by Bergström and Boyce (1998). However, a significant drawback of this approach is the difficulty in estimating viscoelastic parameters, which do not directly correspond to the material's linear viscoelasticity. Nevertheless, several authors (Park and Schapery, 1997; Jung and Youn, 1999; Kumar et al., 2019; Li et al., 2021b; Wubuliaisan et al., 2023b) have successfully used propellant linear viscoelastic parameters in their finite strain constitutive equations.

For propellant softening due to matrix dewetting at the filler interfaces, a penalization of the material strain energy density is commonly adopted (Swanson and Christensen, 1983). The only other option involves increasing the volume change due to the presence of porosities (Andrieux et al., 1997). Several damage parameters, as well as damage evolution functions, have been proposed. Moreover, noting that the superimposition of hydrostatic pressure on uniaxial loadings delays damage occurrence, some authors have incorporated this specificity into their damage evolution models (Park and Schapery, 1997; Özüpek and Becker, 1997; Li et al., 2023).

A significant proportion of materials, including concrete, ceramics, graphite, and composites, exhibit asymmetric behavior under tension and compression (Sun et al., 2010), and propellants are no exception (Heuillet, 1992; Tong et al., 2018; Li et al., 2021a). Due to the high content of rigid fillers, it is likely that the material response

is more influenced by the soft binder in tension than in compression (Tong et al., 2018). Furthermore, it is probable that tension and compression do not damage the material equally, necessitating consideration of possible damage-induced asymmetry or an initial asymmetric behavior (Li et al., 2021a) with distinct damage processes in tension and compression.

The current contribution aims to develop thermodynamically consistent general constitutive equations for representing the behavior of propellants, incorporating temperature-dependent finite strain viscoelasticity, softening due to local damage related to strain and pressure states, and tension-compression asymmetry. To validate the proposed model, three sets of data from the literature will be reproduced. The paper is organized as follows: In the next section, we will briefly review the literature that provides experimental evidence on the mechanical behavior of solid propellants to identify the most representative data sets. Following that, the constitutive equations will be detailed: first, by reviewing the finite strain viscoelastic equations; second, by accounting for damage-induced softening; third, by considering the effects of hydrostatic pressure; and finally, by proposing a tension-compression asymmetry. Section 4 presents a comparison between the model and the selected experimental data sets, along with the procedure for fitting the model parameters. Finally, closing remarks conclude the paper.

2. Solid propellant mechanical behavior

A short but rather complete survey on the mechanical testing of solid propellants has been completed in order to highlight the main features any model should include to properly represent the mechanical behavior of these materials. More than three-quarters of the performed tests are uniaxial and essentially uniaxial tension tests, see (Swanson and Christensen, 1983; Park and Schapery, 1997; Özüpek and Becker, 1992, 1997; Jung and Youn, 1999; Xu et al., 2008; Zhang et al., 2018) among others. Note also that few of the uniaxial loadings are uniaxial compression tests (Yang et al., 2016; Li et al., 2021a; Zhang et al., 2022). Moreover, non-uniaxial tension tests are mainly uniaxial tests with a superimposed hydrostatic pressure (Traissac et al., 1995; Park and Schapery, 1997; Özüpek and Becker, 1997; Li et al., 2021b), the remaining tests covering simple shear (Heuillet, 1992; Picquart, 2020), poker chip tension (Picquart, 2020) and equibiaxial tension loadings (Jung et al., 2000; Nevière, 2006; Wang et al., 2022). Monotonic loadings are also dominant, representing more than half of the tests. One may find monotonic uniaxial tension tests at several strain rates (Park and Schapery, 1997; Özüpek and Becker, 1997; Jung and Youn, 1999; Tunç and Özüpek, 2017) and temperatures (Park and Schapery, 1997; Jung

and Youn, 1999). A few cyclic loadings are also reported (Özüpek and Becker, 1997; Jung and Youn, 1999; Yun et al., 2016; Tunç and Özüpek, 2017). Finally, the linear viscoelasticity is generally characterized either by relaxation tests (Jung and Youn, 1999; Yun et al., 2016; Tunç and Özüpek, 2017) or dynamic mechanical analysis (Park and Schapery, 1997; Nevière, 2006), these materials are prone to satisfy the time-temperature superposition principle (Nevière, 2006).

Propellants may undergo finite strain and Figure 1 illustrates the responses of a hydroxyl-terminated polybutadiene (HTPB) propellant submitted to monotonic tensile tests at several temperatures and strain rates.

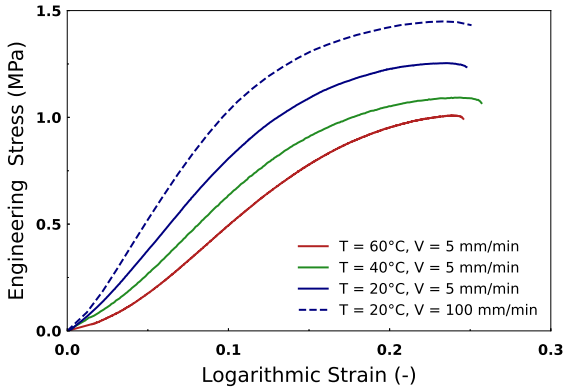

Figure 1: Stress-strain response of a HTPB propellant submitted to monotonic uniaxial tension tests at several temperatures and strain rates.

The concave shape of the stress-strain responses is due to the material softening, resulting from dewetting of the polymer binder from the energetic fillers (Cornwell and Schapery, 1975; Oberth and Bruenner, 1965; Tao et al., 2013; Toulemonde et al., 2016; de Francqueville et al., 2021). Figure 2 shows a scanning electron microscope (SEM) observation of the binder debonding from the fillers with polymer fibrils remaining upon the damage process.

The addition of a superimposed hydrostatic pressure delays damage initiation, leading to higher stress and greater stretch at failure. The positive effect of such pressure saturates at about 5 MPa for HTPB propellants (Bihari et al., 2021; Wang and Qiang, 2022) and 7 MPa for nitrate ester plasticized polyether (NEPE) propellants (Li et al., 2020).

Lastly, due to the high filler volume fraction and the mechanical contrast between the soft binder and rigid fillers, an asymmetric behavior in tension and compression is likely. Consequently, the latter loading state has drawn increased interest recently, either to study the impact of strain rate (Yang et al., 2016; Zhang et al., 2022) or to

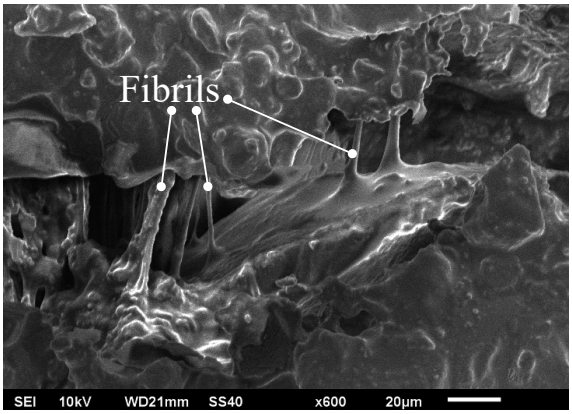

Figure 2: SEM image of damage at the filler interface recorded on a HTPB propellant upon loading.

assess material asymmetry (Li et al., 2021a).

In light of this survey, we have selected three contributions from the literature (Park and Schapery, 1997; Jung and Youn, 1999; Li et al., 2021a) for their relative completeness and representativeness of the mechanical behavior of solid propellants. It should be emphasized that data from (Park and Schapery, 1997; Jung and Youn, 1999) are commonly used as references in the propellant literature. Experimental tests from (Park and Schapery, 1997) were performed on an HTPB propellant and include relaxation master curves of the Young modulus, as well as monotonic uniaxial tension tests at various strain rates, temperatures, and hydrostatic pressures. Data from (Jung and Youn, 1999) were also obtained on an HTPB propellant and provide a similar dataset, except for the uniaxial tests with hydrostatic pressure, but include cyclic uniaxial tension tests with several loading paths. Finally, to validate the model's applicability for tension-compression asymmetry, we have selected data presenting both tension (Li et al., 2021b) and compression (Li et al., 2021a) stress-strain responses obtained on the same material, a NEPE propellant.

3. Modeling

In what follows, vectors are underlined and boldface letters are used to define second-order tensors. Particularly, the identity second-order tensor is written as $\mathbf{I}$, the displacement of a material point $M(\underline{X})$ as $\underline{u}(\underline{X})$, and ∇ stands for the gradient operator, $\nabla\bullet = \frac{\partial \bullet}{\partial \underline{X}}$. In addition, the constitutive equations are expressed in a conventional orthonormal basis.

3.1. Finite strain viscoelastic general equations

As shown previously, propellant materials exhibit large strain time-dependent responses upon loading. A common practice to model such a behavior is to work in a finite strain kinematic framework with the deformation gradient tensor, $\mathbf{F} = \mathbf{I} + \nabla \underline{u}$, satisfying to the classic multiplicative decomposition (Sidoroff, 1974),

$$\mathbf{F} = \mathbf{F}_e \, \mathbf{F}_v, \tag{1}$$

where subscripts e and v stand for the elastic and the viscous parts respectively. On this issue, note that a reversed decomposition $\mathbf{F}_v \, \mathbf{F}_e$ is also possible (Latorre and Montáns, 2016). It is also common to use a volumetric-isochoric decomposition (Flory, 1961; Ogden, 1976). The volume change is denoted $J = \det(\mathbf{F})$, and we may write the isochoric part of the deformation gradient tensor as $\bar{\mathbf{F}} = J^{-1/3}\mathbf{F} = (J_e J_v)^{-1/3}\mathbf{F}_e\mathbf{F}_v$, assuming the hydrostatic part may also show viscoelasticity. The symmetric right Cauchy-Green tensor $\mathbf{C}$ and its isochoric part $\bar{\mathbf{C}}$ write as,

$$\mathbf{C} = \mathbf{F}^T \, \mathbf{F} \quad \text{and} \quad \bar{\mathbf{C}} = \bar{\mathbf{F}}^T \, \bar{\mathbf{F}}. \tag{2}$$

Finally, the isochoric part of the elastic right Cauchy-Green tensor may be defined as,

$$\bar{\mathbf{C}}_e = \bar{\mathbf{F}}_v^{-T} \, \bar{\mathbf{C}} \, \bar{\mathbf{F}}_v^{-1}. \tag{3}$$

Using this kinematic framework, constitutive equations of finite strain viscoelasticity have been written in detail in several contributions, such as (Le Tallec et al., 1993; Lion, 1997; Reese and Govindjee, 1998). Therefore, only the necessary equations to compute the model will be recalled here.

Considering the thermodynamics laws (Coleman and Gurtin, 1967), the material strain energy density $\mathcal{W}$ must satisfy to the Clausius-Duhem inequality,

$$\frac{1}{2}\mathbf{S} : \dot{\mathbf{C}} - \dot{\mathcal{W}} \geq 0, \tag{4}$$

with $\mathbf{S}$ the second Piola-Kirchhoff tensor that relates to the Cauchy stress tensor $\boldsymbol{\sigma}$ and the first Piola-Kirchhoff stress tensor $\mathbf{P}$ through $\boldsymbol{\sigma} = J^{-1}\mathbf{P}\mathbf{F}^T = J^{-1}\mathbf{F}\mathbf{S}\mathbf{F}^T$. From Eq. (4) derives the stress-strain relationship,

$$\mathbf{S} = 2\frac{\partial \mathcal{W}}{\partial \mathbf{C}}, \tag{5}$$

and, the internal dissipation rate inequality,

$$-\sum_i \frac{\partial \mathcal{W}}{\partial \mathbf{A}^i} : \dot{\mathbf{A}}^i \geq 0, \tag{6}$$

with $\mathbf{A}^i$ defining all the material internal variables characterizing dissipative processes such as viscoelasticity or damage. It is worth noting that the latter inequality is usually satisfied in a strong way by verifying that,

$$\forall i, \quad \frac{\partial \mathcal{W}}{\partial \mathbf{A}^i} : \dot{\mathbf{A}}^i \geq 0. \tag{7}$$

Given the rubbery polymer that binds the fillers in propellants, one may adopt the additive decomposition of the strain energy density into its hydrostatic part, $\mathcal{U}$, and its isochoric part, $\bar{\mathcal{W}}$, represented as $\mathcal{W}(\mathbf{F}) = \mathcal{U}(J) + \bar{\mathcal{W}}(\bar{\mathbf{F}})$. Furthermore, the generalized Maxwell model is well-known as an effective framework for representing the viscoelastic behavior of these materials. Such a scheme consists of an elastic branch, denoted here noted ∞, in parallel with n viscoelastic Maxwell branches. Accordingly, the strain energy density representative of such a scheme may thus write as,

$$\mathcal{W}(\mathbf{F}, \mathbf{F}_v^1, ..., \mathbf{F}_v^n) = \mathcal{U}_\infty(J) + \bar{\mathcal{W}}_\infty(\bar{\mathbf{F}}) + \sum_{i=1}^{n} \left(\mathcal{U}_i(J_e^i) + \bar{\mathcal{W}}_i(\bar{\mathbf{F}}_e^i) \right), \tag{8}$$

which may transform into,

$$\mathcal{W}(\mathbf{C}, \mathbf{C}_v^1, ..., \mathbf{C}_v^n) = \mathcal{U}_\infty(J) + \bar{\mathcal{W}}_\infty(\bar{\mathbf{C}}) + \sum_{i=1}^{n} \left(\mathcal{U}_i(J_e^i) + \bar{\mathcal{W}}_i(\bar{\mathbf{C}}_e^i) \right). \tag{9}$$

due to frame indifference. Additionally, for isotropic materials, the dependencies of $\bar{\mathcal{W}}_\infty$ and $\bar{\mathcal{W}}_i$ on $\bar{\mathbf{C}}$ and $\bar{\mathbf{C}}_e^i$, respectively, simplify to dependencies solely on their invariants.

The choice of the state variable evolution is motivated by thermodynamic requirements (Eq. (7)). A comparison conducted by Gouhier and Diani (2024) of pioneering finite strain viscoelastic models within the same framework (Le Tallec et al., 1993; Reese and Govindjee, 1998; Lion, 1997) reveals that, despite different choices of internal variables, their resulting viscoelastic rate equations are similar when expressed in uniform notation. This result holds for both isochoric and hydrostatic parts when the latter is considered. Furthermore, one may note that constitutive equations written independently in (Le Tallec et al., 1993) and (Reese and Govindjee, 1998) linearize well into the infinitesimal strain viscoelastic equations. Therefore, we adopt their proposed formulation for the rate equation governing the isochoric viscoelastic internal variables,

$$\forall i, \quad \dot{\bar{\mathbf{C}}}_v^i = \frac{2}{\eta_d^i} \bar{\mathbf{F}}_v^{i\,T} \operatorname{dev} \left(\frac{\partial \bar{\mathcal{W}}_i}{\partial \bar{\mathbf{C}}_e^i} \bar{\mathbf{C}}_e^i \right) \bar{\mathbf{F}}_v^i, \tag{10}$$

and the simplest evolution for J_v^i,

$$\forall i, \quad \dot{J}_v^i = \frac{J}{\eta_h^i} \frac{\partial \mathcal{U}_i}{\partial J_e^i}. \tag{11}$$

The parameters η_d^i and η_h^i represent the deviatoric and hydrostatic viscosities of the i-th Maxwell branch, respectively. Given that the binder is an amorphous polymer network, the number of Maxwell branches can be determined based on the polymer's linear viscoelastic properties (Nguyen et al., 2008; Arrieta et al., 2014). Furthermore, the time-temperature shift factors established in the linear viscoelastic regime are also applicable to finite strains (Diani et al., 2015), provided that temperature or strain rate conditions do not induce plastic deformations.

3.2. Isotropic damage

To account for the stress softening observed in propellants, it is common practice to apply a penalization to the strain energy density,

$$\mathcal{W}_D(\mathbf{C}, \mathbf{C}_v^1, ..., \mathbf{C}_v^n) = (1 - D_h)\, \mathcal{U}\left(J, J_e^1, ..., J_e^n\right) + (1 - D_d)\, \bar{\mathcal{W}}(\bar{\mathbf{C}}, \bar{\mathbf{C}}_v^1, ..., \bar{\mathbf{C}}_v^n), \tag{12}$$

where D_d and D_h are the internal variables characterizing the deviatoric and hydrostatic damages. Note that, under this approach, both the elastic and viscoelastic components are equally affected by the damage for identification purposes. Although this study does not address it, alternative damage functions that affect either component differently are feasible but would require additional experimental investigations to elucidate the specific damage mechanisms involved.

On the other hand, it is worth mentioning that Andrieux et al. (1997) introduced in hyperelasticity a modified Jacobian, $\tilde{J} = J/g(D)$, depending on a damage function $g(D)$, and wrote,

$$\mathcal{W}_D(\mathbf{C}) = \mathcal{U}(\tilde{J}) + (1 - D)\, \bar{\mathcal{W}}(\bar{\mathbf{C}}). \tag{13}$$

Note that it is possible to use separate internal variables, D_h and D_d, instead of a single variable D for hydrostatic and deviatoric damage, respectively. In doing so, the main difference between these approaches is that the latter induces residual hydrostatic strain, whereas the former does not.

The damage internal variables, D_x with $x \in \{d, h\}$, reflect irreversible processes that likewise the other internal variables must satisfy to Eq. (7),

$$-\frac{\partial \mathcal{W}}{\partial D_x}\, \dot{D}_x \geq 0. \tag{14}$$

They are often defined as $f(\alpha_x^m)$, where α_x^m is the maximum value of a variable α_x over the loading history,

$$\alpha_x^m(t) = \max_{\tau\in[0,t]} \alpha_x(\tau), \tag{15}$$

and f must satisfy to $\partial f/\partial\alpha_x \geq 0$. Thereafter, the complete damage evolution writes as,

$$\dot{D}_x = \begin{cases} \dfrac{df(\alpha_x)}{d\alpha_x}\dot{\alpha}_x & \text{when } \alpha_x - \alpha_x^m = 0 \text{ and } \dot{\alpha}_x > 0 \ , \\ 0 & \text{otherwise.} \end{cases} \tag{16}$$

More specifically, for the deviatoric damage D_d, several forms of f may be found in the literature, such as exponential (Simo, 1987; Miehe, 1995), sigmoïd (Ogden and Roxburgh, 1999) or hyperbolic tangent (Beatty and Krishnaswamy, 2000) functions. The exponential form,

$$f(\alpha_x^m) = 1 - e^{-b_x(\alpha_x^m - \alpha_x^0)^{a_x}}, \quad \alpha_x^0 = \alpha_x(t=0), \tag{17}$$

has been chosen in the current contribution since it brings flexibility with only two parameters, a_x and b_x.

Regarding the definition of the deviatoric damage variable α_d, several expressions have been proposed over the past few decades. On the rubber side, one may cite the strain energy density of the undamaged material (Simo, 1987; Miehe, 1995) as well as the damaged strain energy (Machado et al., 2012), functions of the strain invariants $\bar{I}_1$ and $\bar{I}_2$ of $\bar{\mathbf{C}}$ (Beatty and Krishnaswamy, 2000; Chagnon et al., 2004) or the second invariant $\bar{h}_{eq}$ of the Hencky strain tensor $\bar{\mathbf{h}} = \frac{1}{2}\ln\left(\bar{\mathbf{F}}\,\bar{\mathbf{F}}^T\right)$ that measures the strain amplitude (Merckel et al., 2012). On the solid propellant side, one finds the equivalent strain $\sqrt{\mathrm{tr}(\bar{\mathbf{C}}^T\bar{\mathbf{C}})}$ (Özüpek and Becker, 1992) or the octahedral shear strain $\bar{I}_\gamma = \frac{1}{6}\sqrt{2\,\bar{I}_1^2 - 6\,\bar{I}_2}$ (Özüpek and Becker, 1997).

3.3. Account for a superimposed pressure

As discussed in section 2, the application of hydrostatic pressure in addition to uniaxial loading delays material damage. To address this effect, Özüpek and Becker (1997) incorporated the hydrostatic pressure P_h into the evolution of their damage variable, as follows,

$$\dot{\alpha}_x(P_h) = \dot{\alpha}_x(0)\, e^{P_h/\omega_x^1}, \tag{18}$$

where $\dot{\alpha}_x(0)$ is the damage variable rate when hydrostatic pressure effects are not considered and ω_x^1 a dimensionless material parameter. Their model has been successfully applied in several studies (Jung and Youn, 1999; Jung et al., 2000; Canga

et al., 2001; Yun et al., 2016; Tunç and Özüpek, 2016, 2017; Wubuliaisan et al., 2023b). However, it has been pointed out recently (Li et al., 2023) that due to the simple exponential form, the expression cannot account for a saturation pressure (Traissac et al., 1995). Consequently, Li et al. (2023) have proposed an alternative empirical formulation,

$$\dot{\alpha}_x(P_h) = \dot{\alpha}_x(0)\left(1 - \omega_x\left(1 - e^{-\frac{P_h}{P_s}}\right)\right), \tag{19}$$

where ω_x is a dimensionless material parameter, and P_s is directly deduced from the saturation pressure measured experimentally as shown in (Li et al., 2023). It has been calculated at 1.2 and 2.0 MPa for HTPB and NEPE propellants showing saturation pressure at 5 and 7 MPa, respectively.

It is important to note that in the aforementioned studies, Özüpek and Becker (1997) used the hydrostatic pressure experienced by the material, defined as $P_h = -\frac{1}{3}\mathrm{tr}(\sigma)$, while Li et al. (2023) employed the constant applied pressure. The authors believe that P_h should represent the hydrostatic pressure undergone by the material to define a three-dimensional model applicable to various loading conditions and suitable for implementation in finite element codes.

3.4. Symmetric and asymmetric strain energy densities

While many options are offered by the rubber literature for expressions of $\bar{\mathcal{W}}$ when the material responses are supposed symmetric in tension vs. compression, the simple Neo-Hookean density,

$$\bar{\mathcal{W}}(\bar{\mathbf{C}}, \bar{\mathbf{C}}_e^1, ..., \bar{\mathbf{C}}_e^n) = \sum_{j=1}^{3} \frac{\mu_\infty}{2}\left(\left(\bar{\lambda}_j\right)^2 - 1\right) + \sum_{i=1}^{n}\sum_{j=1}^{3} \frac{\mu_e^i}{2}\left(\left(\bar{\lambda}_{ej}^i\right)^2 - 1\right), \tag{20}$$

with $\left(\bar{\lambda}_j\right)^2$ and $\left(\bar{\lambda}_{ej}^i\right)^2$ the eigenvalues of the isochoric right Cauchy-Green tensors $\bar{\mathbf{C}}$ and $\bar{\mathbf{C}}_e^i$, is usually enough for the representation of propellants (Jung and Youn, 1999; Yun et al., 2016; Kantor et al., 2021; Wubuliaisan et al., 2023a).

To address asymmetric responses in tension compared to compression, recent developments in finite strain elastic energy densities have primarily focused on biological tissues. These models often employ a bi-modulus approach, which assigns different moduli for tension and compression (Zhang et al., 2019; Latorre and Montáns, 2020; Du et al., 2020). Moerman et al. (2016) proposed a method that incorporates the invariants of a specific class of strain tensors, rather than the Green-Lagrange tensor, using a weighting factor to manage asymmetry similarly to bi-modulus models. Additionally, asymmetric viscohyperelastic strain energy densities have been developed (Samadi-Dooki and Voyiadjis, 2019; Zhu et al., 2019), with Zhu et al. (2019)

addressing asymmetry in the elastic component alone using the same path as (Moerman et al., 2016), while Samadi-Dooki and Voyiadjis (2019) extended this approach to both viscous and elastic components.

To account for asymmetric responses, we have extended the model from Du et al. (2020) by reformulating their strain energy expression as follows,

$$\bar{\mathcal{W}}(\bar{\mathbf{C}}, \bar{\mathbf{C}}_e^1, ..., \bar{\mathbf{C}}_e^n) = \sum_{j=1}^{3} \frac{\mu_j}{2} \left(\bar{\lambda}_j^2 - 1 - \ln\left(\bar{\lambda}_j^2\right)\right) + \sum_{i=1}^{n} \left[\sum_{j=1}^{3} \frac{\mu_{ej}^i}{2} \left({\bar{\lambda}_{ej}^i}^2 - 1 - \ln\left({\bar{\lambda}_{ej}^i}^2\right)\right)\right]. \tag{21}$$

It is worth noting that beyond the fact the original model was written within hyperelasticity only, we have modified it by replacing λ_i by $\bar{\lambda}_i$ in the expression Eq. (1) of (Du et al., 2020) since the latter induces couplings between the deviatoric and hydrostatic responses. The shear bi-modulus criteria is then defined as,

$$\mu_j = \begin{cases} \mu_\infty^t & \text{if } \bar{\lambda}_j \geq 1, \\ \mu_\infty^c & \text{if } \bar{\lambda}_j < 1, \end{cases} \qquad \text{and} \qquad \mu_{ej}^i = \begin{cases} \mu_e^{i\,t} & \text{if } \bar{\lambda}_{ej}^i \geq 1, \\ \mu_e^{i\,c} & \text{if } \bar{\lambda}_{ej}^i < 1. \end{cases} \tag{22}$$

Furthermore, when considering propellants with microstructures that are heavily filled with nearly rigid particles, the bi-modulus concept can be extended to account for hydrostatic loads, by writing,

$$\mathcal{U}(J, J_e^1, ..., J_e^n) \;=\; \frac{K_\infty^{tc}}{2}(J-1)^2 + \sum_{i=1}^{n} \frac{K_e^{i\,tc}}{2}(J_e^i - 1)^2 \tag{23}$$

with the following criteria for the bulk bi-modulus,

$$K_\infty^{tc} = \begin{cases} K_\infty^t & \text{if } J \geq 1, \\ K_\infty^c & \text{if } J < 1, \end{cases} \qquad \text{and} \qquad K_e^{i\,tc} = \begin{cases} K_e^{it} & \text{if } J_e^i \geq 1, \\ K_e^{ic} & \text{if } J_e^i < 1. \end{cases} \tag{24}$$

Note that mathematical expression $\mathcal{U}(J) = \dfrac{K}{2}(J-1)^2$ is common for close to incompressible rubbers, as it is implemented in Abaqus finite element code, and may be applied for $\mathcal{U}_\infty$ and $\mathcal{U}_i$. However, if the material becomes compressible, such an expression is unsatisfactory as it does not verify $\mathcal{U}(J) \to \infty$ when $J \to 0$. In such a case, other expressions should be favored for $\mathcal{U}$ like in (Doll and Schweizerhof, 2000).

Propellants may exhibit asymmetric behavior from the outset (Li et al., 2021a), and damage may either induce or exacerbate this asymmetry. This can be expressed

as,

$$\mu_j = \begin{cases} \mu_\infty^t (1 - D_d^t) & \text{if } \bar{\lambda}_j \geq 1, \\ \mu_\infty^c (1 - D_d^c) & \text{if } \bar{\lambda}_j < 1, \end{cases} \tag{25}$$

It is worth noting that introducing distinct damage functions D_d^t and D_d^c in tension and compression, is possible without breaking the material isotropy. The model proposed in Eq. (25) defines only the elastic shear modulus. To easily limit the number of parameters when viscoelasticity is considered, it is therefore recommended to write for the viscoelastic parameters,

$$\mu_{ej}^i = \begin{cases} \beta^{it} \mu_\infty^t (1 - D_d^t) & \text{if } \bar{\lambda}_{ej}^i \geq 1, \\ \beta^{ic} \mu_\infty^c (1 - D_d^c) & \text{if } \bar{\lambda}_{ej}^i < 1, \end{cases} \tag{26}$$

with $\beta^{it} = \mu_e^{it}/\mu_\infty^t$ and $\beta^{ic} = \mu_e^{ic}/\mu_\infty^c$. We will apply this definition to the symmetric case as well, where $\beta^{it} = \beta^{ic}$, simplifying to β^i. When data are available, the parameters β^i can be estimated from the infinitesimal strain viscoelasticity characterization, as $\beta^i = G_i/G_\infty$, with G_∞ the long-term shear modulus and G_i the shear modulus associated with each Maxwell branch in the generalized Maxwell representation. This choice is made to facilitate the identification of material parameters, given the lack of experimental data to support an alternative approach. For each viscoelastic branch, the viscosity η^i is considered constant, independent of the strain state, and Eqs. (10) and (11) continue to apply.

Although not addressed in this study, an asymmetric adjustment to the bulk modulus, analogous to the modifications made for the shear moduli in Eqs. (25) and (26), could also be considered. For instance, one might reasonably account for the effect of matrix debonding at the fillers, which could influence the material's hydrostatic response under tension alone.

3.5. Constitutive equations summary

In the end, by introducing expressions Eqs. (21) and (23) in Eq. (12), and considering the evolution Eqs. (10) and (11) for the viscoelastic internal variables, and the damage definitions Eq. (17) and (19), one may estimate the stress, Eq. (5), solving

the set of equations written below in a tensorial form,

$$
\left\{
\begin{array}{l}
\underline{\textit{Stress-strain relationship}} \\[2ex]
\boldsymbol{\sigma} = (1-D_h)\left(\dfrac{\partial \mathcal{U}_\infty(J)}{\partial J} + \displaystyle\sum_{i=1}^{n} \frac{J_e^i}{J}\frac{\partial \mathcal{U}_i(J_e^i)}{\partial J_e^i}\right)\mathbf{I} \\[2ex]
\quad + (1-D_d)\,\dfrac{2}{J}\,\mathrm{dev}\left(\bar{\mathbf{F}}\,\dfrac{\partial \bar{\mathcal{W}}_\infty(\bar{\mathbf{C}})}{\partial \bar{\mathbf{C}}}\,\bar{\mathbf{F}}^T\right) \\[2ex]
\quad + (1-D_d)\,\dfrac{2}{J}\displaystyle\sum_{i=1}^{n}\mathrm{dev}\left(\bar{\mathbf{F}}_e\,\dfrac{\partial \bar{\mathcal{W}}_i(\bar{\mathbf{C}}_e^i)}{\partial \bar{\mathbf{C}}_e^i}\,\bar{\mathbf{F}}_e^T\right) \\[2ex]
\underline{\textit{Evolution equations of viscoelastic internal variables}} \\[2ex]
\forall i,\ \dot{\bar{\mathbf{C}}}_v^i = \dfrac{2}{\eta_d^i}\,\bar{\mathbf{F}}_v^{i\,T}\,\mathrm{dev}\left(\dfrac{\partial \bar{\mathcal{W}}_i}{\partial \bar{\mathbf{C}}_e^i}\,\bar{\mathbf{C}}_e^i\right)\bar{\mathbf{F}}_v^i \quad \text{and} \quad \dot{J}_v^i = \dfrac{J}{\eta_h^i}\dfrac{\partial \mathcal{U}_i}{\partial J_e^i}, \\[2ex]
\underline{\textit{Damage variables}} \\[2ex]
D_d = 1-e^{-b_d(\alpha_d^m-\alpha_d^0)^{a_d}} \quad \text{and} \quad D_h = 1-e^{-b_h(\alpha_h^m-\alpha_h^0)^{a_h}}, \quad \alpha_x^m = \max(\alpha_x), \\[2ex]
\alpha_d \in \left\{\max_i(\bar{\lambda}_i),\ \sqrt{\frac{\bar{I}_1}{3}}-1,\ \sqrt{\mathrm{tr}(\bar{\mathbf{C}}^T\,\bar{\mathbf{C}})},\ \bar{I}_\gamma,\ \bar{h}_{eq},\ \frac{1}{2}\int \mathbf{S}:\mathrm{d}\mathbf{C}\right\}, \\[2ex]
\dot{\alpha}_x(P_h) = \dot{\alpha}_x(0)\left(1-\omega_x\left(1-e^{-\frac{P_h}{P_s}}\right)\right) \ \text{ with } \ x\in\{d,h\}.
\end{array}
\right. \tag{27}
$$

In this system, the deviator operator is defined as $\mathrm{dev}(\mathbf{X}) = \mathbf{X} - \frac{1}{3}\mathrm{tr}(\mathbf{X})$, while the elastic $\bar{\mathcal{W}}_\infty$ and viscous $\bar{\mathcal{W}}_i$ parts of the isochoric strain energy density are defined either by Eq. (20) for traction/compression symmetric responses, or Eq. (21) otherwise.

Such a constitutive model provides considerable flexibility, which increases with the number of parameters included. However, experimental constraints and modeling simplifications allow for a reduction in the number of parameters without sacrificing representativeness. Specifically, although both hydrostatic and deviatoric components of the strain energy could theoretically require the same number of parameters, such comprehensive versatility is rarely supported by available data. For

instance, we did not find experimental evidence necessitating going further than treating the bulk modulus as a constant elastic parameter, K_∞. Similarly, asymmetric behavior is typically captured solely through the shear modulus, as hydrostatic tension loading is not usually accessible and uniaxial tension/compression primarily influences the deviatoric part. Additionally, assuming D_h to be null throughout loading ensures uncoupled hydrostatic and deviatoric damage processes, simplifying parameter identification. In this context, the deviatoric strain energy is characterized by the long-term shear modulus μ_∞, a viscoelastic spectrum defined by n parameter pairs $(\tau_i, \mu_e^i) = (\tau_i, \beta^i \mu_\infty)$ related to the polymer binder's viscoelasticity (with $\eta_i = \tau_i \, \mu_e^i$), two deviatoric damage parameters a_d and b_d, and two parameters for pressure dependence, P_s and ω_d. Moreover, when asymmetry is accounted for, only the long-term shear modulus μ_∞ is adjusted accordingly. As a result, modeling tension/compression asymmetry introduces one additional long-term shear modulus (Eq. (22)) and two extra damage parameters if this asymmetry is induced or enhanced by damage (Eq. (25)).

Finally, the experimental data sets fitted under finite strain were limited to uniaxial tension, uniaxial tension combined with hydrostatic compression, and uniaxial compression. Consequently, a simple Python script, described in detail in Appendix A, was necessary.

4. Results

In this section, the model is tested on selected data from (Park and Schapery, 1997; Jung and Youn, 1999; Li et al., 2021a), which effectively illustrate the mechanical behavior of solid propellants. As the model is applied, we will describe the estimation of material parameters and propose a parameter fitting procedure. Note that experimental data are depicted by symbols in the figures, while simulations are represented by lines.

4.1. Strain rate dependent responses in uniaxial tension

To facilitate the viscoelasticity characterization of their propellants, Jung and Youn (1999) conducted stress relaxation tests, while Park and Schapery (1997) performed dynamic mechanical analysis, both at infinitesimal strain, to construct shear or Young's modulus relaxation master curves. We employed 16 Maxwell branches, as proposed by Jung and Youn (1999), to fit both sets of data. Figure 3 demonstrates satisfactory agreement between the linear fit and the experimental data. The parameters of the linear fit, including the elastic long-term shear modulus G_∞, and the 16 relaxation times and corresponding moduli (τ_i, G_i), where $G_i = \beta_i \, G_\infty$, are detailed in Appendix B, which lists all the model parameter values.

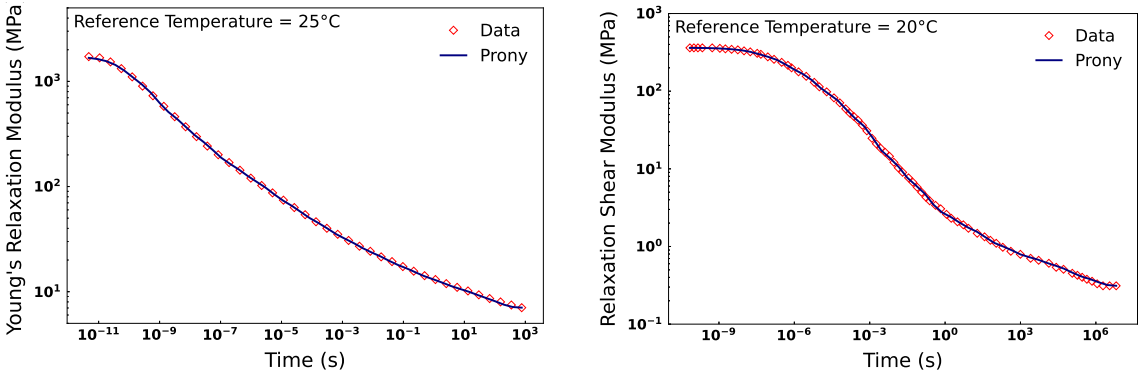

Figure 3: Fit with a 16 branches generalized Maxwell model of the relaxation modulus master curves from (a) Park and Schapery (1997) and (b) Jung and Youn (1999).

Due to the presence of rigid fillers, the binder experiences highly heterogeneous strain fields even at low macroscopic strains. Consequently, the shear modulus μ_∞ at finite strain differs from the infinitesimal strain shear modulus G_∞ (Luo et al., 2023). Therefore, μ_∞ must be fitted using finite strain data, while the parameters (μ_e^i) in Eqs. (20) and (21) and viscosities (η_d^i) in Eq.(10), are now defined as $(\beta_i\mu_\infty)$ and $(\tau_i\mu_e^i)$, respectively. To achieve this, μ_∞ is fitted to the initial portion of the uniaxial tension finite strain responses, under the assumption that no damage has occurred. We employ stress-strain responses obtained at four different strain rates at the temperature where the viscoelastic spectrum was estimated from the relaxation master curve. The values of μ_∞ are also provided in Appendix B.

The damage parameters a_d and b_d from Eq. (17) are then determined to achieve the best fit of the stress-strain responses up to failure. Given that data under applied hydrostatic pressure are available in (Park and Schapery, 1997), the hydrostatic pressure effect parameter ω_d can be calibrated alongside the damage parameters and incorporated into the damage rate equation (Eq. (19)). In contrast, due to the absence of such experimental data in (Jung and Youn, 1999), the damage is assumed to be independent of hydrostatic pressure, as precise calibration of ω_d is not feasible.

To demonstrate the impact of selecting the damage variable α_d in Eq. (27), Figure 4 presents the best fits to the data from Park and Schapery (1997) achieved using six different variables. As anticipated, comparing the model solely against uniaxial tension data does not sufficiently distinguish between these damage variables, as they all yield relatively satisfactory results. The evolution of the deviatoric damage is illustrated in Figure 5 for the responses shown in Figure 4e when the damage vari-

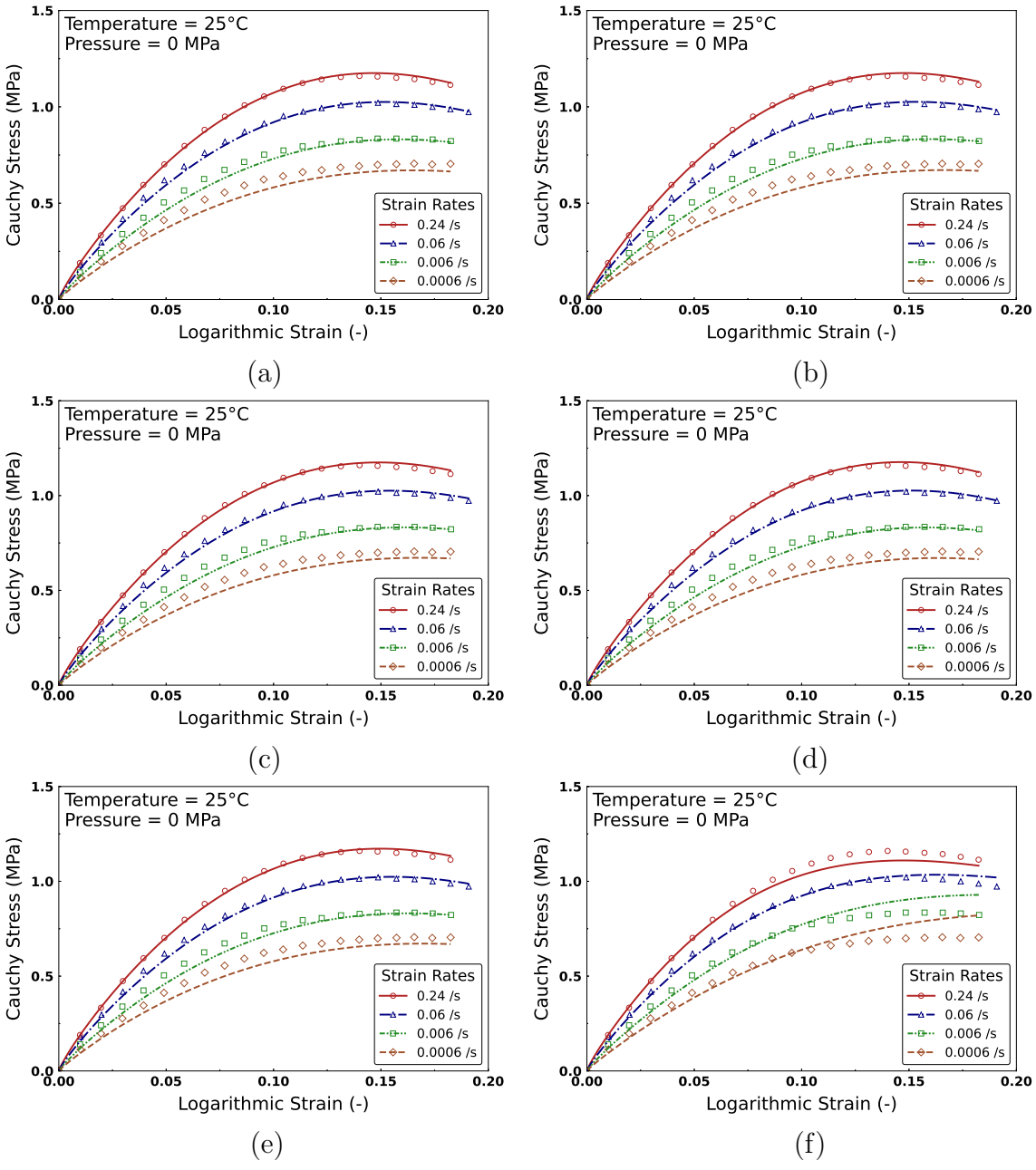

Figure 4: Model best fits for the finite strain uniaxial tension strain-rate dependent responses from (Park and Schapery, 1997) for several damage variables α_d: (a) $\max_i(\bar{\lambda}_i)$, (b) $\sqrt{\bar{I}_1/3-1}$, (c) $\sqrt{\mathrm{tr}(\bar{\mathbf{C}}^T\,\bar{\mathbf{C}})}$, (d) $\bar{I}_\gamma$, (e) $\bar{h}_{eq}$ and (f) $\frac{1}{2}\int \mathbf{S} : d\mathbf{C}$.

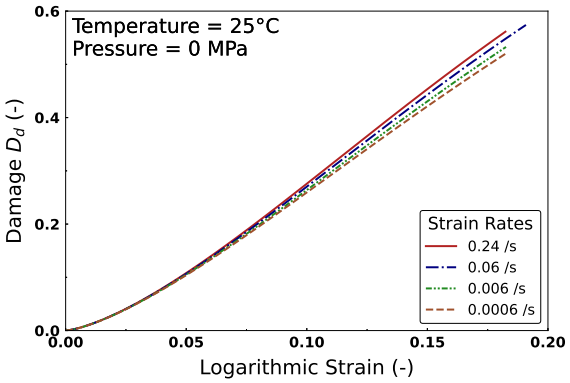

Figure 5: Evolution of deviatoric damage D_d corresponding to the uniaxial tension responses presented in Figure 4e for which $\bar{h}_{eq}$ is the damage variable.

able is $\bar{h}_{eq}$. As expected, higher strain rates result in increased damage, and similar trends have been observed for the other damage variables evaluated in Figure 4.

Figure 6 presents the best fits to the data from Park and Schapery (1997) and Jung and Youn (1999), achieved using the second strain invariant of the Hencky strain tensor for (Park and Schapery, 1997), and the damaged strain energy for (Jung and Youn, 1999).

Furthermore, the representativeness of the model is evaluated in Figure 7 by replicating the uniaxial cyclic responses reported by (Jung and Youn, 1999) using the parameters calibrated in Figure 6b. In line with the experimental data, the left plot depicts the cyclic responses at a constant peak strain of 20% under an imposed strain rate of 8.33×10^{-3}/s, while the right plot illustrates cyclic responses with progressively increasing strain levels, specifically 3, 6, 9, 12, 15 and 20% at a strain rate of 8.33×10^{-4}/s. It is important to note that volume changes were not available for these loadings, so the results are presented using engineering stress. Although the model reproduces the overall cyclic behavior of the material (Figure 7), it is worth mentioning that the better fit reported by (Jung and Youn, 1999) was achieved only by incorporating a phenomenological high-order polynomial fitting function to account for the cyclic damage.

4.2. Temperature-dependent behavior

To account for a change of temperature, we propose to simply apply the time-temperature superposition principle. Consequently, the viscohyperelastic response at another temperature T is just calculated with the parameters identified at the reference temperature T_{ref}, multiplying the relaxation times τ_i by $10^{a_{T_{ref}}(T)}$. The

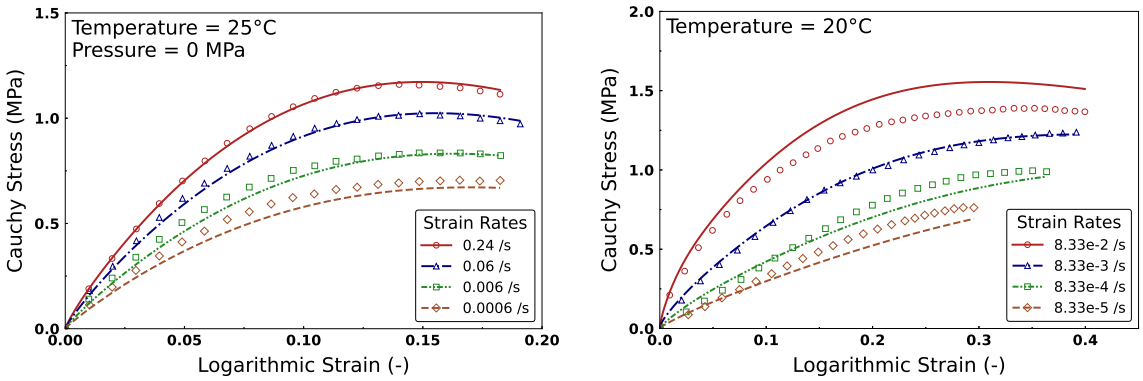

Figure 6: Model representation of the uniaxial tension strain-rate dependent responses of two HTPB propellants from (a) Park and Schapery (1997) and (b) Jung and Youn (1999).

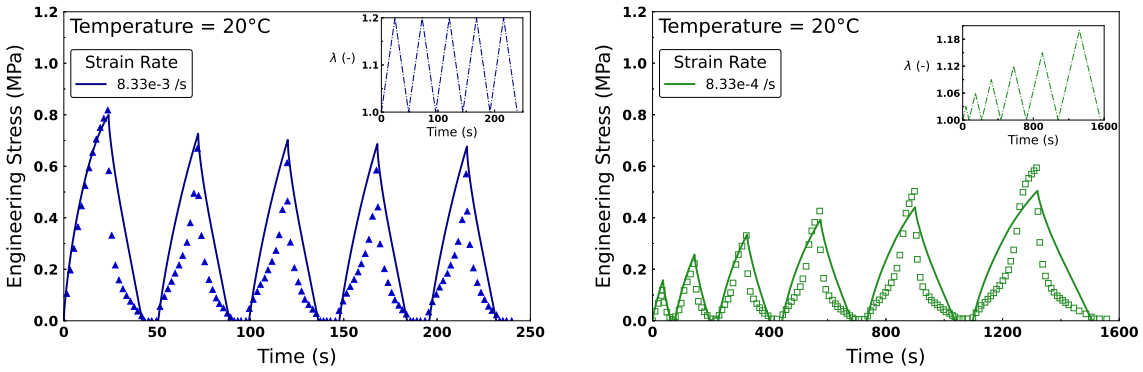

Figure 7: Comparisons of experimental cyclic responses by Jung and Youn (1999) and model cyclic responses calculated with parameters fitted in Figure 6.

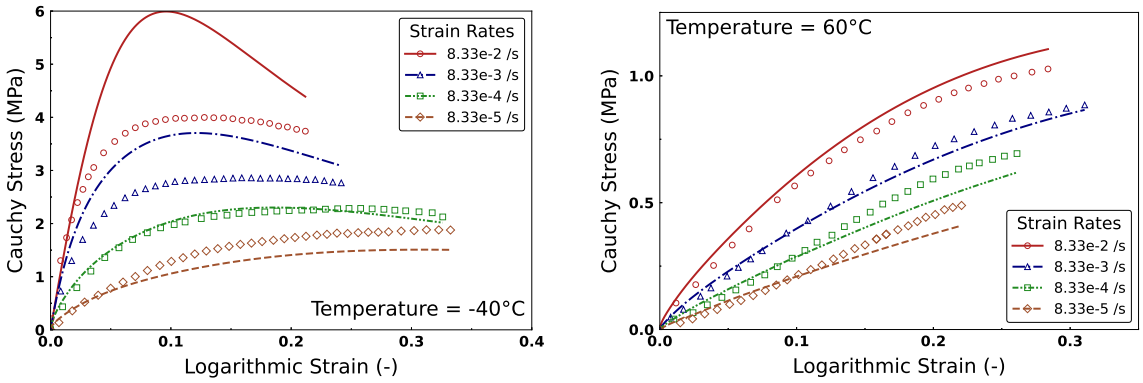

Figure 8: Comparison between experiments (Jung and Youn, 1999) and the model prediction of the temperature-dependent uniaxial tension responses.

shift factors $a_{T_{ref}}(T)$ were simply obtained when building the master curves at infinitesimal strain. The values resulting from the master curves in Figure 3 can be easily approached by the WLF (Williams et al., 1955) equation as one can read in Figure B.15.

Therefore, without additional fitted parameters, the uniaxial tension responses reported at other temperatures are reproduced in Figure 8. While the stress-strain responses at high temperatures are well reproduced, the model shows some limitations at low temperatures and higher strain rates, which is not surprising since the matrix is getting closer to the glassy state where the possible extension of the infinitesimal strain time-temperature superposition principle to finite strain remains to be explored (Diani et al., 2015).

4.3. Material response with superimposed hydrostatic pressure

In use, solid propellant rocket engines are subjected to internal pressure, which is why uniaxial tension tests with superimposed hydrostatic pressure are commonly conducted on these materials. Section 3.3 explains how hydrostatic pressure should be incorporated into the damage evolution model to accurately reproduce uniaxial tension responses under pressure. For comparison, both damage rate formulations, Eqs. (18) and (19), were tested in Figure 9, which shows uniaxial tension responses at a constant strain rate of 0.24/s under various superimposed pressures. As previously discussed, the value of P_h in these equations represents the hydrostatic pressure applied to the material, evaluated as $-K_\infty(J-1)$ during loading. Notably, the second approach, Eq. (19), which accounts for a saturation pressure, provides a better fit, particularly at higher confining pressures. While the model performs very

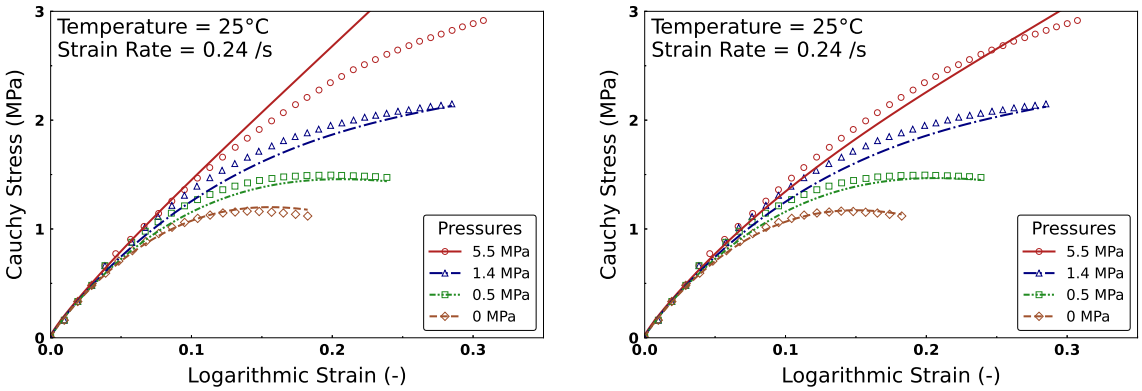

Figure 9: Comparison of the account for superimposed hydrostatic pressure according to Eq. (18) (left) and Eq. (19) (right) against experimental data from (Park and Schapery, 1997).

well at moderate pressures, some room for improvement remains at higher pressures, despite a qualitatively satisfactory trend.

Additional evaluations of the model's capability to account for superimposed pressures are presented in Figures 10 and 11, where the data from (Li et al., 2021a) have been accurately reproduced for uniaxial compression. Since the authors did not characterize the linear viscoelasticity of their material, the relaxation times and corresponding stiffnesses β_i were estimated from the uniaxial stress-strain compression responses at strains below 10%, under the assumption that no damage had yet occurred. A good fit for the strain rate dependence (Figure 10a) was achieved using 8 Maxwell branches, which are detailed in Appendix B.3. Subsequently, assuming that the propellants behave as incompressible materials under uniaxial compression, the damage parameters a_d, b_d, and ω_d were calibrated using true stress-strain compression curves at various strain rates without applied pressure (Figure 10a), and at different pressures with a constant strain rate of 6.67×10^{-2}/s (Figure 10b). The model's representativeness for these estimations is further validated by its performance at various strain rates under an imposed pressure of 2 MPa (Figure 11).

4.4. Tension/Compression asymmetrical behavior

As discussed in Section 2, experimental data encompassing both tension and compression tests are limited. To evaluate the significance of incorporating asymmetric behavior, we have selected monotonic uniaxial tension tests (Li et al., 2021b) and monotonic uniaxial compression tests (Li et al., 2021a), both conducted on the same material across various strain rates. It is important to note that for the uniaxial compression tests, the authors assumed incompressibility when plotting Cauchy stress

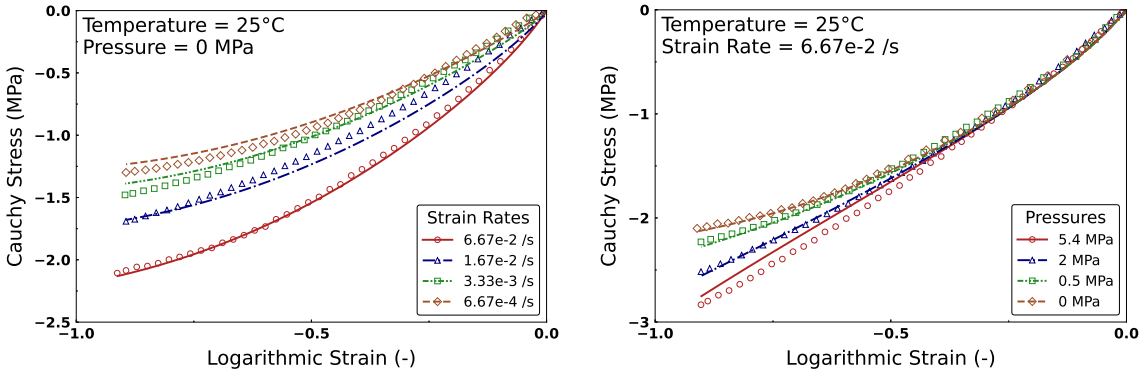

(a) (b)

Figure 10: Model representations of a NEPE uniaxial compression responses (a) at various strain rates with no imposed pressure and (b) at various pressures with imposed strain rate of 6.67×10^{-2}/s (Li et al., 2021a).

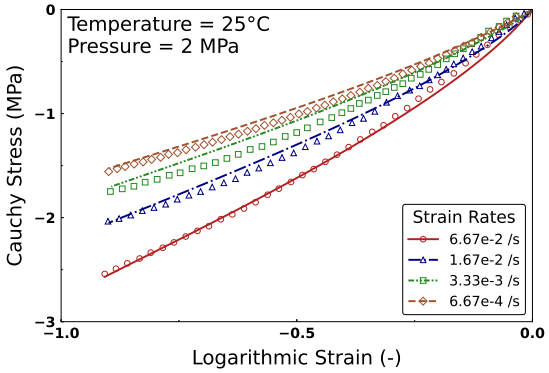

Figure 11: Model representations of a NEPE uniaxial compression responses at various strain rates with imposed pressure of 2 MPa (Li et al., 2021a).

values, and volume change data are unavailable for the uniaxial tension tests. Consequently, the results are presented using logarithmic strain and engineering stress.

Initially, with the assumption of identical parameters for both tension and compression, material parameters were fitted based on uniaxial tension data and subsequently applied to replicate the compression tests (Figure 12). It must be emphasized that the representation of compression behavior was limited to moderate strain because, at large strains, the behavior of propellants under such loading conditions resembles that of granular materials, which likely falls outside the scope of the current model. Additionally, the viscoelastic parameters employed in this study are consistent with those reported by Li et al. (2021b) and are detailed in Appendix B.4. In this context, the relaxation times and corresponding stiffnesses β_i were characterized within the linear viscoelastic regime using a simple relaxation test, incorporating only three viscoelastic Maxwell branches. Figure 12 also illustrates a satisfactory representation of the damaged behavior in tension, achieved by utilizing the strain amplitude invariant of the Hencky tensor as the damage variable. However, the compression responses were significantly underestimated. Similar results were obtained when the damage parameters were derived from compression data, and the model was subsequently tested in tension. Finally, it should be noted that the viscoelastic spectrum identified in uniaxial tension does not fully capture the compressive behavior across various strain rates. However, this observation aligns with the distinct viscoelastic spectra used to model tensile and compressive behaviors as reported in (Li et al., 2021a,b).

On the other hand, distinct initial moduli for compression and tension, μ_∞^c and μ_∞^t, along with distinct damage parameters D_d^c and D_d^t, were optimized to accurately capture both tension and compression responses simultaneously. The results of this optimization are shown in Figure 13, where the second invariant of the Hencky tensor was retained once again as the damage variable. The improved representation supports the assumption of asymmetry. However, to further validate the model's asymmetry, it would be valuable in future studies to subject propellants to sequences of tension followed by compression, and vice versa.

5. Conclusions

After reviewing the propellant literature to identify the main features of their mechanical behavior, a three-dimensional, damageable finite strain viscoelastic model with possible tension-compression asymmetry has been proposed within a thermodynamically consistent framework. The model was then tested against reference data from the literature. It has been shown to perform well for uniaxial stress-strain

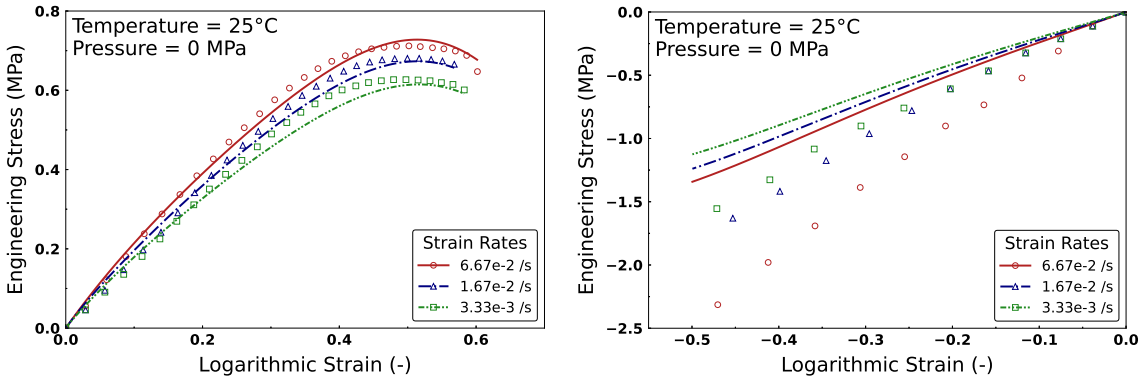

Figure 12: Symmetric tension-compression model representations of the finite strain viscoelastic uniaxial behavior under (a) tension and (b) compression (Li et al., 2021a,b) when parameters are fitted on uniaxial tension.

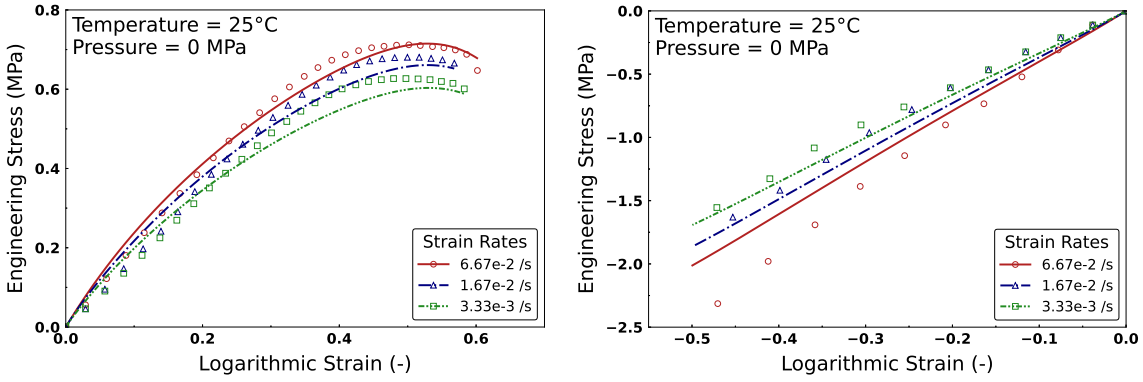

Figure 13: Asymmetric tension-compression model representations of the finite strain viscoelastic uniaxial behavior under (a) tension and (b) compression (Li et al., 2021a,b) when parameters are fitted on both sets of data.

responses at different strain rates and temperatures, including cases where hydrostatic pressure was superimposed. Additionally, a step-by-step procedure for fitting parameters has been proposed. First, the viscoelasticity and time-temperature superposition parameters are classically characterized using linear viscoelasticity data. Next, an initial finite strain stiffness parameter is fitted for the undamaged material, leaving only four damage parameters to be adjusted. These parameters are fitted to account for material softening. When considering the damage dependence on hydro-

static pressure, the four resulting damage parameters are simultaneously estimated based on uniaxial stress-strain responses at different strain rates under the same temperature and hydrostatic pressure, as well as at different constant applied pressures with the same temperature and strain rate.

Despite the good representativeness of the model, this work could be extended in the future in at least three aspects. During the model presentation, it was noted that several damage variables are possible. However, the lack of comprehensive experimental data involving non-proportional or non-uniaxial loadings hinders the identification of the most appropriate variable. Furthermore, the initial effort to account for material asymmetry presented here has also been constrained by the limited availability of experimental data exploring this aspect in greater detail. For instance, tests involving uniaxial compression following uniaxial tension, or uniaxial tension following uniaxial compression, rather than conducting uniaxial compression tests independently of uniaxial tension tests, should be considered. Additionally, more data from cyclic tests, as opposed to monotonic loadings, could improve the accuracy of damage estimation. Finally, further tests involving hydrostatic loadings are necessary to better understand the impact of matrix debonding on the bulk modulus under both hydrostatic tension and compression.

Acknowledgement

The authors are grateful to ArianeGroup SAS, Centre de Recherches du Bouchet, Vert-le-Petit (France), and the Délégation Générale de l'Armement (DGA) for their financial support.

Appendix A. Numerical implementation

This appendix aims to present the constitutive equations and the numerical scheme employed to compute the model responses, as well as the optimization method used in the fitting procedure.

Appendix A.1. Integration algorithm

The constitutive equations of interest are the uniaxial version of Eq. (27). The kinematic of such loading is defined through the deformation gradient tensors,

$$\mathbf{F} = \begin{pmatrix} J^{1/3}\bar{\lambda} & & \\ & \frac{J^{1/3}}{\sqrt{\bar{\lambda}}} & \\ & & \frac{J^{1/3}}{\sqrt{\bar{\lambda}}} \end{pmatrix} \quad \text{and} \quad \bar{\mathbf{F}} = \begin{pmatrix} \bar{\lambda} & & \\ & \frac{1}{\sqrt{\bar{\lambda}}} & \\ & & \frac{1}{\sqrt{\bar{\lambda}}} \end{pmatrix}, \tag{A.1}$$

with $\dot{\lambda} = \frac{d(J^{1/3}\bar{\lambda})}{dt}$ representing the input strain rate from the experimental tests and serving as the sole control variable. The isochoric stretch rate is thus defined as,

$$\dot{\bar{\lambda}} = \frac{\dot{\lambda}}{J^{1/3}} - \frac{1}{3}\frac{\dot{J}}{J}\bar{\lambda}. \tag{A.2}$$

The decomposition $\bar{\lambda} = \bar{\lambda}_e\bar{\lambda}_v$ drives to,

$$\bar{\mathbf{F}}_v^i = \begin{pmatrix} \bar{\lambda}_v^i & & \\ & \frac{1}{\sqrt{\bar{\lambda}_v^i}} & \\ & & \frac{1}{\sqrt{\bar{\lambda}_v^i}} \end{pmatrix} \quad \text{and} \quad \bar{\mathbf{C}}_e^i = \begin{pmatrix} (\bar{\lambda}_e^i)^2 & & \\ & \frac{1}{\lambda_e^i} & \\ & & \frac{1}{\lambda_e^i} \end{pmatrix}. \tag{A.3}$$

Now, by recalling the constitutive assumptions outlined in section 3.5 and the symmetric hydrostatic and deviatoric strain energy densities described in section 3.4,

the relevant equations from Eq. (27) can be reformulated as follows,

$$
\left\{
\begin{array}{l}
\underline{\textit{Uniaxial stress-strain relationships}} \\[2ex]
\textcircled{\text{H}} : \forall i,\ K_e^i = 0, \quad \text{then} \quad \sigma_h = \dfrac{\partial \mathcal{U}}{\partial J} = K_\infty\,(J-1), \\[2ex]
\sigma_{11} = \sigma_h + \dfrac{2}{3J}(1-D_d)\left\{\mu_\infty\left(\bar{\lambda}^2 - \dfrac{1}{\bar{\lambda}}\right) + \displaystyle\sum_{i=1}^{n}\mu_e^i\left((\bar{\lambda}_e^i)^2 - \dfrac{1}{\bar{\lambda}_e^i}\right)\right\}, \\[2ex]
\sigma_{22} = \sigma_{33} = 0 \\
\qquad = \sigma_h + \dfrac{1}{3J}(1-D_d)\left\{\mu_\infty\left(\dfrac{1}{\bar{\lambda}} - \bar{\lambda}^2\right) + \displaystyle\sum_{i=1}^{n}\mu_e^i\left(\dfrac{1}{\bar{\lambda}_e^i} - (\bar{\lambda}_e^i)^2\right)\right\}, \\[2ex]
\underline{\textit{Evolution equations of viscoelastic internal variables}} \\[2ex]
\forall i,\ \dot{\bar{\lambda}}_v^i = \dfrac{\mu_e^i}{3\eta_d^i}\left((\bar{\lambda}_e^i)^2 - \dfrac{1}{\bar{\lambda}_e^i}\right)\bar{\lambda}_v^i, \quad \text{and} \quad \dot{J}_v^i = 0, \\[2ex]
\underline{\textit{Damage variables}} \\[2ex]
D_d = 1 - e^{-b_d(\alpha_d^m - \alpha_d^0)^{a_d}} \quad \text{and} \quad D_h = 0, \quad \alpha_d^m = \max(\alpha_d), \\[2ex]
\alpha_d \in \left\{\max_i(\bar{\lambda}_i),\ \sqrt{\tfrac{\bar{I}_1}{3}} - 1,\ \sqrt{\mathrm{tr}(\bar{\mathbf{C}}^T\,\bar{\mathbf{C}})},\ \bar{I}_\gamma,\ \bar{h}_{eq},\ \tfrac{1}{2}\int \mathbf{S} : \mathrm{d}\mathbf{C}\right\}, \\[2ex]
\dot{D}_d = \begin{cases} \dfrac{df(\alpha_d)}{d\alpha_d}\dot{\alpha}_d & \text{when } \alpha_d - \alpha_d^m = 0 \text{ and } \dot{\alpha}_d > 0\ , \\[2ex] 0 & \text{otherwise,} \end{cases} \\[2ex]
\dot{\alpha}_d(P_h) = \dot{\alpha}_d(0)\left(1 - \omega_d\left(1 - e^{-\frac{P_h}{P_s}}\right)\right).
\end{array}
\right. \tag{A.4}
$$

The unknowns λ, $\bar{\lambda}$, J, and n viscoelastic internal variables $\bar{\lambda}_v^i$, which are necessary to determine the stress response, are defined by a system of differential equations,

which is conventionally expressed as,

$$\mathbf{y} = \begin{bmatrix} \lambda \\ \bar{\lambda} \\ J \\ \bar{\lambda}_v^0 \\ \vdots \\ \bar{\lambda}_v^n \end{bmatrix} \qquad \Longrightarrow \qquad \dot{\mathbf{y}} = \frac{d\mathbf{y}}{dt} = \begin{bmatrix} \dot{\lambda} \\ \dot{\bar{\lambda}} \\ \dot{J} \\ \dot{\bar{\lambda}}_v^0 \\ \vdots \\ \dot{\bar{\lambda}}_v^n \end{bmatrix} \tag{A.5}$$

While $\dot{\lambda}$ is the stretch rate applied to the specimen, and $\dot{\bar{\lambda}}$ and $\dot{\bar{\lambda}}_v^i$ are determined by Eqs (A.2) and (A.4), respectively, $\dot{J}$ is obtained by solving the derivative of the stress-free components, such that,

$$\forall t, \quad \dot{\sigma}_{22} = \dot{\sigma}_{33} = 0 \quad \Longrightarrow \quad \dot{J} = \mathcal{F}(\bar{\lambda}, J, \dot{\bar{\lambda}}_v^0, \ldots, \dot{\bar{\lambda}}_v^n), \tag{A.6}$$

where $\mathcal{F}$ is given as,

$$\begin{cases} \text{Numerator}^{\infty} = \dfrac{\mu_\infty}{3J}\left(1 - D_d\right)\left(2\bar{\lambda} + \dfrac{1}{\bar{\lambda}^2}\right)\dot{\bar{\lambda}} - \dfrac{\mu_\infty}{3J}\,\dot{D}_d\left(\bar{\lambda}^2 - \dfrac{1}{\bar{\lambda}}\right) \\ \text{Denominator}^{\infty} = K_\infty + \dfrac{\mu_\infty}{3J^2}\left(1 - D_d\right)\left(\bar{\lambda}^2 - \dfrac{1}{\bar{\lambda}}\right) \\ \text{Numerator}^{i} = \dfrac{\mu_e^i}{3J}\left(1 - D_d\right)\left(2(\bar{\lambda}\bar{\Lambda}^i) + \dfrac{1}{(\bar{\lambda}\bar{\Lambda}^i)^2}\right)\left(\dot{\bar{\lambda}}\bar{\Lambda}^i + \bar{\lambda}\dot{\bar{\Lambda}}^i\right) \\ \qquad\qquad - \dfrac{\mu_e^i}{3J}\,\dot{D}_d\left((\bar{\lambda}\bar{\Lambda}^i)^2 - \dfrac{1}{(\bar{\lambda}\bar{\Lambda}^i)}\right) \\ \text{Denominator}^{i} = \dfrac{\mu_e^i}{3J^2}\left(1 - D_d\right)\left((\bar{\lambda}\bar{\Lambda}^i)^2 - \dfrac{1}{(\bar{\lambda}\bar{\Lambda}^i)}\right) \\ \qquad \Longrightarrow \quad \dot{J} = \dfrac{\text{Numerator}^e + \sum_i^n \text{Numerator}^i}{\text{Denominator}^e + \sum_i^n \text{Denominator}^i}, \end{cases} \tag{A.7}$$

adopting the notation $\bar{\Lambda}^i = 1/\bar{\lambda}_v^i$ for readability purposes.

To solve the system of nonlinear differential equations in Eq. (A.5), a Python script was developed using the `solve_ivp` solver with the `LSODA` integration method from the `scipy.integrate` package. Such an integration algorithm computes the updated values of the solution vector, $\mathbf{y}_{t=t_{n+1}}$, for a generic time interval $[t_n, t_n + 1]$, based on the solutions $\mathbf{y}_{t=t_n}$ and $\dot{\mathbf{y}}_{t=t_n}$ from the previous time step t_n. The update is performed using the following approach:

$$\mathbf{y}_{t=t_{n+1}} = \texttt{solve\_ivp}\left\{\dot{\mathbf{y}}_{t=t_{n+1}}(\mathbf{y}_{t=t_n}, \dot{\mathbf{y}}_{t=t_n}), [t_n, t_n + 1], \texttt{method} = \texttt{LSODA}\right\} \tag{A.8}$$

It should be emphasized that the details provided in this section are formulated for the symmetric deviatoric strain energy density (Eqs. (20) and (23)), given that the implementation of the asymmetric deviatoric strain energy density, as defined in Eq. (21), follows an analogous procedure.

Appendix A.2. Optimization method

The material parameters requiring identification can be categorized into two groups: the viscoelastic spectrum, which is defined through a Prony series and calibrated based on the relaxation modulus master curve, and the damage parameters, including a_d, b_d, ω_d and P_s (the latter of which is typically determined from the material properties). The optimization methods employed to identify these parameters are summarized below.

- Identification of the viscoelastic parameters

  The viscoelastic spectra for the experimental data from Park and Schapery (1997) and Jung and Youn (1999) were identified using the `pyvisco` package (Springer, 2022).

- Identification of the damage parameters

  As outlined in section 3.3, the confining pressure delays damage progression, making the damage evolution dependent on $P_h = -\frac{1}{3}\text{tr}(\boldsymbol{\sigma})$. Consequently, the three damage parameters $\theta = [a_d, b_d, \omega_d]$ are interrelated and have been calculated using a Monte Carlo optimization approach to fit the set of experimental data according to the least squares criterion.

Appendix B. Model parameters

The model parameters used to fit each set of experimental data are listed here. Due to the inherent difficulties in experimentally characterizing the viscoelasticity of the bulk modulus, it is important to recall that the latter has been assumed to be an elastic constant.

Appendix B.1. Parameters to fit data from Park and Schapery (1997)

Figure B.14a shows the log values of shift factor $a_{T_{ref}}(T)$ and an approximation by the WLF function,

$$\log a_{T_{ref}}(T) = \frac{-C_1\,(T - T_{ref})}{C_2 + (T - T_{ref})} \tag{B.1}$$

where T_{ref} is the reference temperature at which the shift factor have been evaluated, and the parameters $C_1 = 5.5$ and $C_2 = 155.6°\text{C}$ have been determined by a mere fit for a reference temperature of 25°C.

Values of a Prony series defined at infinitesimal strain, which provides a satisfactory representation of the Young's relaxation modulus shown in Figure 3a, have been calculated. Considering near incompressibility, the shear modulus is assumed to be one-third of the Young's modulus, and the resulting Prony series for the shear modulus is listed in Table B.1.

The fit of the finite strain responses before damage occurs yielded $\mu_\infty = 0.859\,G_\infty$, and the elastic bulk modulus has been taken as $K_\infty = 1000\,\mu_\infty$.

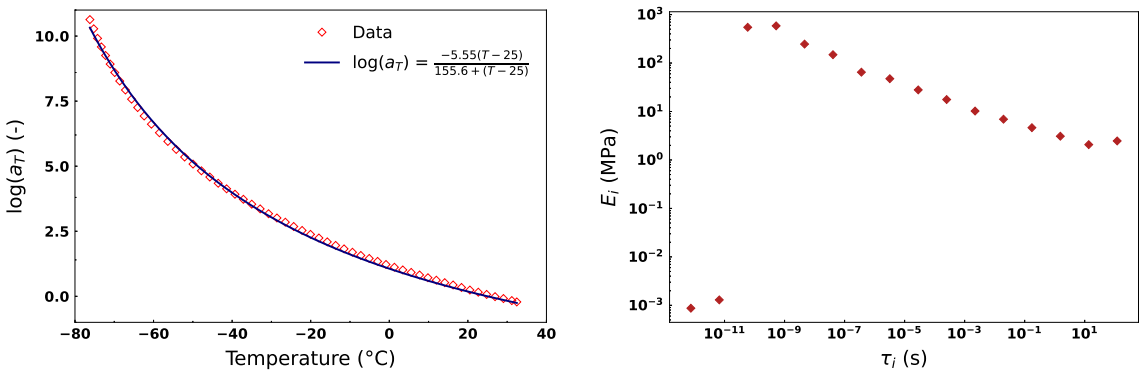

(a) (b)

Figure B.14: (a) WLF fit of the shift factor values obtained by building Park and Schapery (1997) Young's relaxation modulus master curve at infinitesimal strain and (b) Prony series coefficients for the fit of Figure 3a with 16 Maxwell branches.

		$G_\infty = 2.4$ MPa
n	τ_i **(s)**	$\beta_i G_\infty$ **(MPa)**
1	7.56×10^{-13}	0.00029
2	6.69×10^{-12}	0.000432
3	5.92×10^{-11}	182
4	5.24×10^{-10}	195
5	4.64×10^{-09}	82
6	4.11×10^{-08}	49.6
7	3.63×10^{-07}	21.6
8	3.21×10^{-06}	15.8
9	2.84×10^{-05}	9.30
10	2.52×10^{-04}	5.88
11	2.23×10^{-03}	3.41
12	1.97×10^{-02}	2.31
13	1.74×10^{-01}	1.55
14	$1.54 \times 10^{+00}$	1.03
15	$1.37 \times 10^{+01}$	0.691
16	$1.21 \times 10^{+02}$	0.822

Table B.1: Prony series coefficients of the relaxation shear modulus from (Park and Schapery, 1997).

Damage variable α_d	**Parameters**	**Values (-)**	**Usage**
$\max_i(\bar{\lambda}_i)$	a_d b_d	1.35 5.70	Figure 4a
$\sqrt{\bar{I}_1/3} - 1$	a_d b_d	0.70 10.9	Figure 4b
$\sqrt{\mathrm{tr}(\bar{\mathbf{C}}^T \bar{\mathbf{C}})}$	a_d b_d	0.68 2.60	Figure 4c
$\bar{I}_\gamma$	a_d b_d	1.34 8.80	Figure 4d
$\bar{h}_{eq}$	a_d b_d	1.40 6.98	Figures 4e, 5, 6a, 9
$\frac{1}{2}\int \mathbf{S} : d\mathbf{C}$	a_d b_d	0.88 5.90	Figure 4f

Table B.2: Deviatoric damage parameters used to fit experimental data from (Park and Schapery, 1997).

Parameters	**Values**	**Usage**
P_s	1.20 (MPa)	Figures 4, 5, 6a, 9b
ω_d	0.61 (-)	
ω_d^1	-2.3 (-)	Figure 9a

Table B.3: Pressure effect parameters used to fit experimental data from (Park and Schapery, 1997).

Appendix B.2. Parameters to fit data from Jung and Youn (1999)

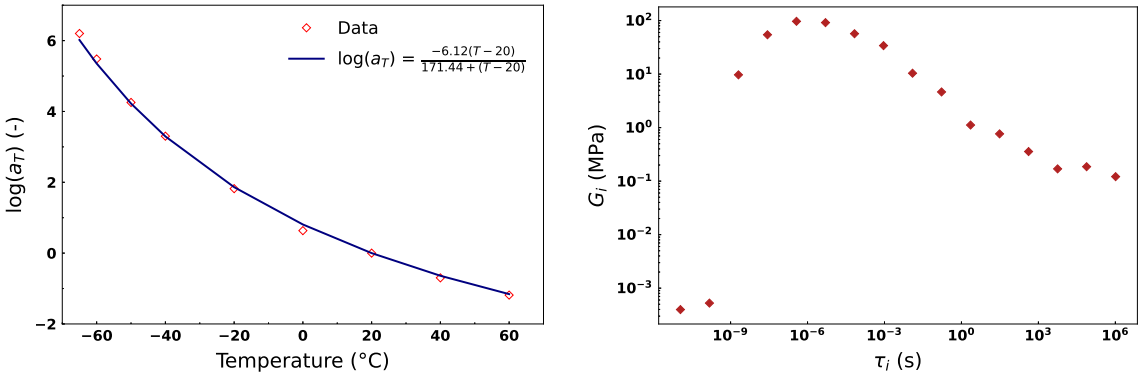

(a) (b)

Figure B.15: (a) WLF fit of the shift factor values obtained by building Jung and Youn (1999) shear relaxation modulus master curve at infinitesimal strain and (b) Prony series coefficients for the fit of Figure 3b with 16 Maxwell branches.

The fit of the finite strain responses before damage occurs resulted in $\mu_\infty = 1.1\,G_\infty$, and the elastic bulk modulus has been set as $K_\infty = 1000\,\mu_\infty$ for this modeling. The WLF parameters $C_1 = 6.12$ and $C_2 = 171.44°\text{C}$ were determined through a mere fit (Figure B.15a) for a reference temperature of 20°C, and these parameters are used via the time-temperature superposition principle to generate the stress-strain curves at different temperatures, as shown in Figure 8. Regarding the damage parameters, it is recalled that the dependence on hydrostatic pressure P_h as described in Eq. (19) was not considered due to the absence of experimental data at various constant pressures, which are necessary to calibrate P_s and ω_d.

		$G_\infty = 0.3$ MPa
n	τ_i **(s)**	$\beta_i G_\infty$ **(MPa)**
1	1.11×10^{-11}	0.000398
2	1.50×10^{-10}	0.000526
3	2.03×10^{-09}	9.69
4	2.74×10^{-08}	54.3
5	3.71×10^{-07}	96.9
6	5.01×10^{-06}	91.6
7	6.78×10^{-05}	56.8
8	9.16×10^{-04}	34
9	1.24×10^{-02}	10.4
10	1.68×10^{-01}	4.64
11	$2.27 \times 10^{+00}$	1.12
12	$3.06 \times 10^{+01}$	0.764
13	$4.14 \times 10^{+02}$	0.357
14	$5.60 \times 10^{+03}$	0.169
15	$7.57 \times 10^{+04}$	0.186
16	$1.02 \times 10^{+06}$	0.121

Table B.4: Prony series coefficients of the relaxation shear modulus from (Jung and Youn, 1999).

Damage variable α_d	**Parameters**	**Values (-)**	**Usage**
$\frac{1}{2}\int \mathbf{S} : d\mathbf{C}$	a_d	2.38	Figures 6b, 7, 8
	b_d	0.52	

Table B.5: Deviatoric damage parameters used to fit experimental data from (Jung and Youn, 1999).

Appendix B.3. Parameters to fit uniaxial compression tests with pressure from (Li et al., 2021a)

		$G_\infty = 0.6$ MPa
n	τ_i **(s)**	$\beta_i G_\infty$ **(MPa)**
1	1.0×10^{-01}	0.033
2	5.0×10^{-01}	0.05
3	$1.0 \times 10^{+00}$	0.533
4	$6.0 \times 10^{+00}$	0.3
5	$1.2 \times 10^{+01}$	0.133
6	$1.0 \times 10^{+02}$	0.116
7	$1.0 \times 10^{+03}$	0.046
8	$1.0 \times 10^{+04}$	0.093

Table B.6: Prony series coefficients of the relaxation shear modulus fitted on uniaxial compression tests at various strain rates and no superimposed pressure from (Li et al., 2021a).

Damage variable α_d	**Parameters**	**Values**	**Usage**
$\bar{h}_{eq}$	a_d	2.38 (-)	Figure 10
	b_d	0.52 (-)	
	P_s	2.0 (MPa)	
	ω_d	0.94 (-)	

Table B.7: Deviatoric damage parameters used to fit experimental data of compression tests at various strain rates and confining pressures from (Li et al., 2021a).

As the viscoelastic spectrum was directly identified from the finite strain responses before the damage occurred, it results in $\mu_\infty = G_\infty$. Note that the elastic bulk modulus has been set to $K_\infty = 1148$ MPa (Li et al., 2021a) for this modeling.

Appendix B.4. Parameters to fit data from (Li et al., 2021a,b)

		$G_\infty = 0.4$ MPa
n	τ_i **(s)**	$\beta_i G_\infty$ **(MPa)**
1	$1.69 \times 10^{+00}$	0.118
2	$2.69 \times 10^{+01}$	0.0743
3	$3.79 \times 10^{+02}$	0.0793

Table B.8: Prony series coefficients of the relaxation shear modulus from (Li et al., 2021b).

The fit of the finite strain responses before the damage occurred resulted in $\mu_\infty^{tc} = 1.22\, G_\infty$ for the symmetric case. In the asymmetric case, the finite shear moduli were directly optimized to yield $\mu_\infty^t = 0.275$ and $\mu_\infty^c = 1.15$. For both compression and tension, $\forall i \in \{1, 3\},\ \eta_i = \tau_i \mu_e^{it}$. Finally, the elastic bulk modulus has been set to $K_\infty = 1148$ MPa (Li et al., 2021a) for both cases in this modeling.

Damage variable α_d	**Parameters**	**Values**	**Usage**
$\bar{h}_{eq}$	a_d^{tc}	5.0 (-)	Figure 12
	b_d^{tc}	3.7 (-)	
	P_s	2.0 (MPa)	
	ω_d	0.94 (-)	

Table B.9: Deviatoric damage parameters in the symmetric case, fitted on tension and compression data from (Li et al., 2021a,b).

Damage variable α_d	**Parameters**	**Values**	**Usage**
$\bar{h}_{eq}$	a_d^t	8.44 (-)	Figure 13
	a_d^c	3.65 (-)	
	b_d^t	15.67 (-)	
	b_d^c	0.95 (-)	
	P_s	2.0 (MPa)	
	ω_d	0.94 (-)	

Table B.10: Deviatoric damage parameters in the asymmetric case, fitted on tension and compression data from (Li et al., 2021a,b).

References

Andrieux, F., Saanouni, K., Sidoroff, F., 1997. Sur les solides hyperélastiques à compressibilité induite par l'endommagement. Comptes Rendus de l'Académie des Sciences - Series IIB - Mechanics-Physics-Chemistry-Astronomy 324, 281–288.

Arrieta, S., Diani, J., Gilormini, P., 2014. Experimental characterization and thermoviscoelastic modeling of strain and stress recoveries of an amorphous polymer network. Mechanics of Materials 68, 95–103.

Beatty, M.F., Krishnaswamy, S., 2000. A theory of stress-softening in incompressible isotropic materials. Journal of the Mechanics and Physics of Solids 48, 1931–1965.

Bergström, J.S., Boyce, M.C., 1998. Constitutive modeling of the large strain time-dependent behavior of elastomers. Journal of the Mechanics and Physics of Solids 46, 931–954.

Bihari, B.P., Kumaraswamy, A., Jain, M., Rao, N.P.N., Murthy, K.P.S., 2021. Effect of pressure on mechanical properties of composite propellant. Propellants, Explosives, Pyrotechnics 46, 799–805.

Canga, M.E., Becker, E.B., Özüpek, Ş., 2001. Constitutive modeling of viscoelastic materials with damage – computational aspects. Computer Methods in Applied Mechanics and Engineering 190, 2207–2226.

Chagnon, G., Verron, E., Gornet, L., Marckmann, G., Charrier, P., 2004. On the relevance of continuum damage mechanics as applied to the Mullins effect in elastomers. Journal of the Mechanics and Physics of Solids 52, 1627–1650.

Coleman, B.D., Gurtin, M.E., 1967. Thermodynamics with internal state variables. The Journal of Chemical Physics 47, 597–613.

Cornwell, L.R., Schapery, R.A., 1975. SEM study of microcracking in strained solid propellant. Metallography 8, 445–452.

Davenas, A., 2003. Development of modern solid propellants. Journal of Propulsion and Power 19, 1108–1128.

Diani, J., Gilormini, P., Arrieta, J., 2015. Direct experimental evidence of time-temperature superposition at finite strain for an amorphous polymer network. Polymer 58, 107–112.

Doll, S., Schweizerhof, K., 2000. On the development of volumetric strain energy functions. Journal of Applied Mechanics 67, 17–21.

Du, Z., Zhang, G., Guo, T., Tang, S., Guo, X., 2020. Tension-compression asymmetry at finite strains: A theoretical model and exact solutions. Journal of the Mechanics and Physics of Solids 143, 104084.

Duncan, E.J.S., Margetson, J., 1998. A nonlinear viscoelastic theory for solid rocket propellants based on a cumulative damage approach. Propellants, Explosives, Pyrotechnics 23, 94–104.

Flory, P.J., 1961. Thermodynamic relations for high elastic materials. Trans. Faraday Soc. 57, 829–838.

de Francqueville, F., Diani, J., Gilormini, P., Vandenbroucke, A., 2021. Use of a micromechanical approach to understand the mechanical behavior of solid propellants. Mechanics of Materials 153, 103656.

Gouhier, F., Diani, J., 2024. A comparison of finite strain viscoelastic models based on the multiplicative decomposition. European Journal of Mechanics - A/Solids 108, 105424.

Govindjee, S., Potter, T., Wilkening, J., 2014. Dynamic stability of spinning viscoelastic cylinders at finite deformation. International Journal of Solids and Structures 51, 3589–3603.

Ha, K., Schapery, R.A., 1998. A three-dimensional viscoelastic constitutive model for particulate composites with growing damage and its experimental validation. International Journal of Solids and Structures 35, 3497–3517.

Heuillet, P., 1992. Caractérisation de l'endommagement des propergols solides composites. Theses. Compiègne.

Jung, G.D., Youn, S.K., 1999. A nonlinear viscoelastic constitutive model of solid propellant. International Journal of Solids and Structures 36, 3755–3777.

Jung, G.D., Youn, S.K., Kim, B.K., 2000. A three-dimensional nonlinear viscoelastic constitutive model of solid propellant. International Journal of Solids and Structures 37, 4715–4732.

Kantor, M.M., Assous, F., Golubchik, A., Hariton, I., Fedulov, B.N., 2021. Three-dimensional constitutive equations for hyper viscoelastic particulate reinforced composite materials based on damage parameter. International Journal of Solids and Structures 229, 111138.

Kumar, N., Patel, B.P., Rao, V.V., Subhaschandran, B.S., 2018. Hyperviscoelastic constitutive modelling of solid propellants with damage and compressibility. Propellants, Explosives, Pyrotechnics 43, 461–471.

Kumar, N., Patel, B.P., Rao, V.V., Subhaschandran, B.S., 2019. Compressibility, damage, and age-hardening effects of solid propellants using finite strain constitutive model. Journal of Engineering Materials and Technology 141, 031001.

Latorre, M., Montáns, F.J., 2016. Fully anisotropic finite strain viscoelasticity based on a reverse multiplicative decomposition and logarithmic strains. Computers & Structures 163, 56–70.

Latorre, M., Montáns, F.J., 2020. Bi-modulus materials consistent with a stored energy function: Theory and numerical implementation. Computers & Structures 229, 106176.

Le Tallec, P., Rahier, C., Kaiss, A., 1993. Three-dimensional incompressible viscoelasticity in large strains: Formulation and numerical approximation. Computer Methods in Applied Mechanics and Engineering 109, 233–258.

Li, H., Wang, S.X., Li, M., Xu, J.S., Fan, X.G., Chen, X., 2020. Experimental research on tensile mechanical properties of NEPE propellant under confining pressure. Propellants, Explosives, Pyrotechnics 45, 1769–1779.

Li, H., Xu, J.S., Chen, X., Hou, Y.F., Fan, X.G., Li, M., Li, H.W., 2021a. Experimental investigation and modeling the compressive behavior of NEPE propellant under confining pressure. Propellants, Explosives, Pyrotechnics 46, 1023–1035.

Li, H., Xu, J.S., Chen, X., Zhang, J.F., Li, J., 2023. A nonlinear viscoelastic constitutive model with damage and experimental validation for composite solid propellant. Scientific Reports 13, 2049.

Li, H., Xu, J.S., Liu, J.M., Wang, T.Y., Chen, X., Li, H.W., 2021b. Research on the influences of confining pressure and strain rate on NEPE propellant: Experimental assessment and constitutive model. Defence Technology 17, 1764–1774.

Lion, A., 1997. A physically based method to represent the thermo-mechanical behaviour of elastomers. Acta Mechanica 123, 1–25.

Luo, H., Hooshmand-Ahoor, Z., Danas, K., Diani, J., 2023. Numerical estimation via remeshing and analytical modeling of nonlinear elastic composites comprising a large volume fraction of randomly distributed spherical particles or voids. European Journal of Mechanics - A/Solids 101, 105076.

Machado, G., Chagnon, G., Favier, D., 2012. Induced anisotropy by the Mullins effect in filled silicone rubber. Mechanics of Materials 50, 70–80.

Merckel, Y., Diani, J., Brieu, M., Gilormini, P., Caillard, J., 2012. Effect of the microstructure parameters on the mullins softening in carbon-black filled styrene–butadiene rubbers. Journal of Applied Polymer Science 123, 1153–1161.

Miehe, C., 1995. Discontinuous and continuous damage evolution in Ogden-type large-strain elastic materials. European Journal of Mechanics A-solids 14, 697–720.

Moerman, K.M., Simms, C.K., Nagel, T., 2016. Control of tension–compression asymmetry in Ogden hyperelasticity with application to soft tissue modelling. Journal of the Mechanical Behavior of Biomedical Materials 56, 218–228.

Nevière, R., 2006. An extension of the time–temperature superposition principle to non-linear viscoelastic solids. International Journal of Solids and Structures 43, 5295–5306.

Nguyen, T.D., Qi, J.H., Castro, F., Long, K.N., 2008. A thermoviscoelastic model for amorphous shape memory polymers: Incorporating structural and stress relaxation. Journal of the Mechanics and Physics of Solids 56, 2792–2814.

Oberth, A.E., Bruenner, R.S., 1965. Tear phenomena around solid inclusions in castable elastomers. Transactions of The Society of Rheology 9, 165–185.

Ogden, R.W., 1976. Volume changes associated with the deformation of rubber-like solids. Journal of the Mechanics and Physics of Solids 24, 323–338.

Ogden, R.W., Roxburgh, D.G., 1999. A pseudo-elastic model for the Mullins effect in filled rubber. Proceedings of the Royal Society of London. Series A: Mathematical, Physical and Engineering Sciences 455, 2861–2877.

Özüpek, Ş., Becker, E.B., 1992. Constitutive modeling of high-elongation solid propellants. Journal of Engineering Materials and Technology 114, 111–115.

Özüpek, Ş., Becker, E.B., 1997. Constitutive equations for solid propellants. Journal of Engineering Materials and Technology 119, 125–132.

Park, S.W., Schapery, R.A., 1997. A viscoelastic constitutive model for particulate composites with growing damage. International Journal of Solids and Structures 34, 931–947.

Picquart, M., 2020. Développement d'une loi de comportement pour les méthodes de dimensionnement des chargements en propergol solide composite. Theses. Université Paris-Saclay.

Reese, S., Govindjee, S., 1998. A theory of finite viscoelasticity and numerical aspects. International Journal of Solids and Structures 35, 3455–3482.

Samadi-Dooki, A., Voyiadjis, G.Z., 2019. A fully nonlinear viscohyperelastic model for the brain tissue applicable to dynamic rates. Journal of Biomechanics 84, 211–217.

Sidoroff, F., 1974. Nonlinear viscoelastic model with an intermediate configuration. J. Mec. 13, 679–713.

Simo, J.C., 1987. On a fully three-dimensional finite-strain viscoelastic damage model: Formulation and computational aspects. Computer Methods in Applied Mechanics and Engineering 60, 153–173.

Springer, M., 2022. PYVISCO: A Python library for identifying Prony series parameters of linear viscoelastic materials. URL: `https://github.com/NREL/pyvisco`, doi:10.5281/zenodo.6384954.

Sun, J.Y., Zhu, H.Q., Qin, S.H., Yang, D.L., He, X.T., 2010. A review on the research of mechanical problems with different moduli in tension and compression. Journal of Mechanical Science and Technology 24, 1845–1854.

Swanson, S.R., Christensen, L.W., 1983. A constitutive formulation for high-elongation propellants. Journal of Spacecraft and Rockets 20, 559–566.

Tao, Z.J., Ping, S.D., Mei, Z., Cheng, Z.P., 2013. Microstructure deformation and fracture mechanism of highly filled polymer composites under large tensile deformation. Journal of Physics: Conference Series 419, 012014.

Tong, X., Chen, X., Xu, J.S., Zheng, Y., Zhi, S.J., 2018. The heat build-up of a polymer matrix composite under cyclic loading: Experimental assessment and numerical simulation. International Journal of Fatigue 116, 323–333.

Toulemonde, P.A., Diani, J., Gilormini, P., Desgardin, N., 2016. On the account of a cohesive interface for modeling the behavior until break of highly filled elastomers. Mechanics of Materials 93, 124–133.

Traissac, Y., Ninous, J., Neviere, R., Pouyet, J., 1995. Mechanical behavior of a solid composite propellant during motor ignition. Rubber Chemistry and Technology 68, 146–157.

Tunç, B., Özüpek, Ş., 2016. Implementation and validation of a three dimensional damaging finite strain viscoelastic model. International Journal of Solids and Structures 102-103, 275–285.

Tunç, B., Özüpek, Ş., 2017. Constitutive modeling of solid propellants for three dimensional nonlinear finite element analysis. Aerospace Science and Technology 69, 290–297.

Wang, Q., Wang, G., Wang, Z., Qiang, H., Wang, X., Li, S., Zhu, Z., 2022. Biaxial tensile test and meso damage numerical simulation of HTPB propellant. Scientific Reports 12, 17635.

Wang, Z.J., Qiang, H.F., 2022. Mechanical properties of thermal aged HTPB composite solid propellant under confining pressure. Defence Technology 18, 618–625.

Williams, M.L., Landel, R.F., Ferry, J.D., 1955. The temperature dependence of relaxation mechanisms in amorphous polymers and other glass-forming liquids. Journal of the American Chemical Society 77, 3701–3707.

Wubuliaisan, M., Wu, Y., Hou, X., 2023a. A unified viscoelastic model of progressive damage and failure for solid propellants. International Journal of Plasticity 170, 103765.

Wubuliaisan, M., Wu, Y., Hou, X., Fenglei, H., 2023b. A viscoelastic constitutive model considering deformation and environmental-induced damages for solid propellants. Aerospace Science and Technology 132, 108055.

Xu, F., Aravas, N., Sofronis, P., 2008. Constitutive modeling of solid propellant materials with evolving microstructural damage. Journal of the Mechanics and Physics of Solids 56, 2050–2073.

Yang, L., Xie, K., Pei, J., Sui, X., Wang, N., 2016. Compressive mechanical properties of HTPB propellant at low, intermediate, and high strain rates. Journal of Applied Polymer Science 133, 43512.

Yun, K.S., Park, J.B., Jung, G.D., Youn, S.K., 2016. Viscoelastic constitutive modeling of solid propellant with damage. International Journal of Solids and Structures 80, 118–127.

Yıldırım, H.C., Özüpek, Ş., 2011. Structural assessment of a solid propellant rocket motor: Effects of aging and damage. Aerospace Science and Technology 15, 635–641.

Zhang, G., Guo, T.F., Guo, X., Tang, S., Fleming, F., Liu, W.K., 2019. Fracture in tension–compression-asymmetry solids via phase field modeling. Computer Methods in Applied Mechanics and Engineering 357, 112573.

Zhang, H.N., Chang, H., Li, X.J., Wu, X.G., He, Q.W., 2022. The effect of strain rate on compressive behavior and failure mechanism of CMDB propellant. Defence Technology 18, 467–475.

Zhang, L., Zhi, S., Shen, Z., 2018. Research on tensile mechanical properties and damage mechanism of composite solid propellants. Propellants, Explosives, Pyrotechnics 43, 234–240.

Zhu, Z., Jiang, C., Jiang, H., 2019. A visco-hyperelastic model of brain tissue incorporating both tension/compression asymmetry and volume compressibility. Acta Mechanica 230, 2125–2135.